Structure of the extracellular region of the adhesion GPCR CELSR1 reveals a compact module which regulates G protein-coupling

Sumit J. Bandekar[1,2,3,4], Krassimira Garbett[5], Szymon P. Kordon[1,2,3,4], Ethan Dintzner[1,2,3,4], Tanner Shearer[5], Richard C. Sando[5,*], and Demet Araç[1,2,3,4,*]

Affiliations

[1]Department of Biochemistry and Molecular Biology, The University of Chicago, Chicago, IL, 60637.

[2]The University of Chicago Neuroscience Institute, The University of Chicago, Chicago, IL, 60637.

[3]Institute for Biophysical Dynamics, The University of Chicago, Chicago, IL, 60637.

[4]Center for Mechanical Excitability, The University of Chicago, Chicago, IL, 60637.

[5]Department of Pharmacology, Vanderbilt Brain Institute, Vanderbilt University, Nashville, TN 37240.

*Corresponding authors: Demet Araç, arac@uchicago.edu and Richard C. Sando, Richard.sando@vanderbilt.edu

Abstract

Cadherin EGF Laminin G seven-pass G-type receptors (CELSRs or ADGRCs) are conserved adhesion G protein-coupled receptors which are essential for animal development. CELSRs have extracellular regions (ECRs) containing 23 adhesion domains which couple adhesion to intracellular signaling. However, molecular-level insight into CELSR function is sparsely available. We report the 4.3 Å cryo-EM reconstruction of the mCELSR1 ECR with 13 domains resolved in the structure. These domains form a compact module mediated by interdomain interactions with contact between the N- and C-terminal domains. We show the mCELSR1 ECR forms an extended species in the presence of Ca^{2+}, which we propose represents the antiparallel cadherin repeat dimer. Using assays for adhesion and G protein-coupling, we assign the N-terminal CADH1-8 module as necessary for cell adhesion and we show the C-terminal CAHD9-GAIN module regulates signaling. Our work provides important molecular context to the literature on CELSR function and opens the door towards further mechanistic studies.

Introduction

Multicellular organisms use an array of cell-surface receptors to facilitate productive adhesion between cells and initiate signaling to control developmental and regulatory processes. The adhesion class of G protein-coupled receptors (aGPCRs) are an understudied family of cell-surface receptors that link adhesion to signaling through their multidomain extracellular regions.[1–3] The aGPCR subfamily of Cadherin EGF Laminin-G seven-pass G-type receptors (CELSRs or ADGRCs) are one of two aGPCR subfamilies conserved as distantly as *C. elegans* and CELSRs are essential for the embryonic and neural development of animals.[4–7] CELSRs are involved in the process of planar cell polarity (PCP)[8–13], where they are key for neural tube closure[8,10,14,15], organization of inner ear stereocilia[8,10] and neuroepithelial cilia[16], lymphatic valve formation[17], and skin hair patterning[8,15]. In the nervous system, CELSRs regulate neuronal migration, dendritic growth, and axon guidance.[18–22] CELSRs are ubiquitously expressed in epithelial cell types during embryonic development.[23–26] During development of the nervous system, CELSRs are highly expressed throughout the CNS.[23–25] Mutations in CELSRs are strongly associated with neural tube defects including spina bifida and craniorachischisis, resulting in a range of physical and intellectual disabilities up to embryonic lethality.[27–31] CELSRs are also associated with lymphedema, Joubert syndrome, Tourette syndrome and leukemia.[32–40]

From their N-termini, CELSRs have poorly conserved prodomains (PRO) with a putative furin cleavage site. Following PRO are nine cadherin repeats (CADH1-9) which take up ~ 40 % of the ECR mass, making CELSRs a unique CADH-containing subfamily of the aGPCRs.[41–43] Cadherin repeats are protein-protein interaction modules with ~ 100 residue globular domains with linker regions that coordinate calcium. Three Ca^{2+} ions bind between two CADH repeats and rigidify this linker and this can include many repeats in tandem. This rigid CADH repeat structure mediates cell adhesion in a specific manner.[44,45] CADH repeats act as 'molecular Velcro' to hold cells together and are mechanotransducers.[46] CELSR1 mutants which change single CADH residues directly involved in coordinating Ca^{2+} result in PCP phenotypes and embryonic lethality.[8] Following the CELSR cadherin

repeats, there is a Flamingo box (Fbox) domain which is unique to CELSR/Flamingo proteins.[13] Fbox domains bear structural homology to the membrane-adjacent domains (MADs) of protocadherins (pCDHs).[47] Furthermore, CELSRs have a similar domain architecture to pCDHs and FAT cadherins, which have a series of CADH repeats, a MAD domain, and either a transmembrane domain (pCDH) or a series of LamG and EGF domains (FAT).[41,43,47–49] pCDHs overlap several N-terminal CADH repeats to dimerize, making tight antiparallel dimers which can serve as mechanotransducers; these proteins are also involved in neuronal self-avoidance.[50–55] MADs can form cis-dimers with an adjacent CADH repeat where the minimal unit of N-CADH-MAD-C is necessary to dimerize.[47] Multiple studies have demonstrated the importance of the CELSR CADH region in cell adhesion, but molecular detail is sparsely available.[11–13,20] A recent report determined low resolution images of the full extracellular region of human CELSR2, showing an extended region likely consisting of the CADH repeats, and a globular region of unknown structure. This study also shows that the CADH repeats likely wrap around each other tightly, using multiple cadherin domains to form tight extended dimer species similar in principle to protocadherins.[56] Another recent study determined crystal structures of CELSR1 CADH1-4 and CADH4-7, giving the first high-resolution insight into the CADH repeat region of CELSR and revealing a non-canonical linker between CADH5 and CADH6.[57]

Next, CELSRs have a series of epidermal growth factor (EGF) and Laminin G (LamG) domains. mCELSR1 has 3 EGF repeats (EGF1-3), the first LamG domain (LamG1), EGF4, LamG2, and EGF5-8. EGF repeats found extracellularly can serve scaffolding functions[58–62] or act as protein-protein interaction (PPI) modules.[63] LamG domains are found in PPI sites such as in Neurexin.[64,65] The ECR ends with the hormone receptor domain (HormR) and GPCR autoproteolysis inducing domain (GAIN). CELSR orthologs across different species variably include the residues for GAIN domain autoproteolysis.[66,67] No function has been demonstrated for this C-terminal EGF/LamG/HormR/GAIN region. The CELSR seven-transmembrane (7TM) region is thought to couple to $G\alpha_s$ and finally, CELSRs have a long intracellular region of about 300 residues.[67]

Despite various hints of CELSR structure and function available in the literature, detailed information at the molecular level about these proteins is minimally present. In addition, mechanistic insight for how CELSRs convert adhesion into signaling remains unavailable. In this work, we determined the 4.3 Å cryogenic electron microscopy (cryo-EM) reconstruction of the mCELSR1 ECR, which revealed a compact multidomain module (CMM) consisting of thirteen domains including CADH9-GAIN. Within this CMM, the N-terminal CADH9 and C-terminal GAIN domain form the primary contact interface using conserved residues. As such, the CADH9-GAIN CMM is likely present across CELSR/Flamingo orthologs. We also report the experimental structure of the Fbox domain within this module. We used biophysical assays to study the full ECR in the presence of Ca^{2+} and we observed an extended species, which we propose represents an intertwined antiparallel dimer found in a configuration similar to protocadherins. We analyzed truncations of mCELSR1, and we show the CADH1-8 module is sufficient for cellular adhesion, and the CADH9-GAIN CMM regulates G protein-coupling. Other aGPCRs have CMMs and therefore CMM may represent a paradigm which maintains specific distance restraints, allows regulation by splice variation, or is sensitive to mechanical force to couple adhesion to signaling.

Results

The cryo-EM reconstruction of the mCELSR1 ECR reveals that the CADH9-GAIN domains form a compact module with N- and C-terminal domains making the primary interface.

We purified the mCELSR1 ECR construct CADH1-GAIN (Supplementary Figure S1 A-C) and we performed single-particle cryo-EM analysis on this construct (Figure 1). Our initial 2D class averages from screening images showed compact triangle-shaped particles about 160 Å in the longest dimension (Supplemental Figure S1 D, E). We also collected images in the presence of $CaCl_2$ but observed strong aggregation and did not pursue (Supplemental Figure S1 F). Processing of a full dataset resulted in a 4.3 Å reconstruction (Figure 1 B, C, Table1, and Supplemental Figure S2) which allowed for unambiguous assignment of the CADH9-GAIN domains within the density map (Figure 1 D-F). The CADH1-8 domains are unresolved in this reconstruction; presumably they are flexible relative to the

CADH9-GAIN module in the absence of Ca^{2+}. They appear in 2D averages as blurry density connected to CADH9 (Supplemental Figure S2).

The thirteen domains in the CADH9-GAIN module form a compact multidomain module (CMM) architecture reminiscent of the ouroboros, an ancient symbol of rebirth where a snake is depicted eating its own tail.[68] The overall dimensions are ~ 160 x 120 x 75 Å. CADH9 forms the 'head' of the snake (Figure 1 E, F), and the GAIN domain is the 'tail'. The CADH9/GAIN interaction surface plays a critical role in stabilizing the module. CADH9, Fbox, EGF1-3, and LamG1 are tightly packed next to each other, occluding the putative LamG1 binding site. EGF4 and LamG2 also form a compact group with the LamG2 canonical binding site accessible for binding partners. Then, EGF5-8 are found in an extended conformation, representing the long body of the snake wrapped around the other domains. EGF5 and EGF6 contact LamG1, and EGF7 contacts EGF2. Finally, EGF8 leads into the HormR domain and the GAIN domain.

Our cryo-EM reconstruction allows us to report the experimental structure of the Fbox domain, a domain type thought to be unique to CELSR/Flamingo orthologs (Supplemental Figure S3 A). [13] We confirm previous work which predicted the Fbox domain to be structurally similar to MAD domains of protocadherins and FAT cadherins as well as the ferredoxin-like domains of nuclear pore proteins.[47,57,69] Using the DALI webserver, we identified several SEA domains as structural homologs of Fbox, including the SEA domain of the aGPCR ADGRG6 (Supplementary Figure S3 A).[70] The CELSR Fbox domain does not have the residues for furin cleavage which some SEA domains have (Supplementary Figure S3 B).[71] The pCDH15 MAD domain forms a dimer with its adjacent CADH repeat, where the CADH of one monomer interacts with the MAD of the other monomer, and vice versa. The orientation of CADH9 to Fbox is different from the CADH11-MAD orientation in pCDH15, and the dimerization surface is sterically hindered within the CELSR CMM (Supplementary Figure S3 C, D).

We can hypothesize how the CADH9-GAIN module is oriented relative to the membrane using our structure supplemented with AlphaFold2 models (Supplemental Figure S3D).[72] A large loop in the GAIN

domain, which is not resolved in our structure, is basic and hydrophobic and could transiently interact with the outer surface of the membrane. Surfaces on EGF2/3 and EGF8 also have surface exposed hydrophobic patches facing the putative plasma membrane. With this orientation, the flat plane of the CADH9-GAIN module is angled about 30 ° from the plasma membrane and the cadherin repeats would project outward at that angle.

The CADH9-GAIN module is largely mediated by interdomain hydrophobic contacts.

Three key interfaces stabilize the CADH9-GAIN module (Figure 2 A). In the CADH9/GAIN interface (Figure 2 B), conserved residues F2188 and Y2250 interact with L1163, L1165, and L1187. Additionally, N1184 on CAHD9 interacts with E2195 on GAIN and R1185 from CADH9 interacts with several backbone carbonyls on GAIN. A salt bridge is observed between E1188 and R2252 as well. A robust hydrophobic core is observed between LAMG2 and EGF5/6 (Figure 2 C). Residues V1581, H1584, F1585, Y1588, V1589, and Y1592 from LAMG1 pack against F1918, V1923, L1928, P1930, Y1947, and Y1959 from EGF6. Also, R1945 packs against D1576 and several backbone carbonyls and D1578 interacts with the hydroxyls of Y1947, Y1959, and N1958. Hydrophobic contacts are also seen between EGF2 and EGF7 (Figure 2 D). I1379 and Y1383 of EGF2 pack against W1972, W1973, V1977, P1980, and H1982 of EGF7.

The mCELSR1 extracellular region forms a Ca^{2+}-dependent dimer with an extended conformation.

We did not observe CADH1-8 domains in our cryo-EM reconstruction even though these domains were about 40 % of the mass of our mCELSR1 construct. CADH repeats have flexible interdomain linkers that rigidify upon Ca^{2+} binding, forming extended species that multimerize.[44,45] In order to resolve the CADH repeats, we biophysically characterized the CADH1-GAIN construct in the absence and presence of Ca^{2+} using size exclusion chromatography coupled to multi-angle light scattering (SEC-MALS) (Figure 3). We observed a leftward shift in the elution volume in the presence of 1 mM $CaCl_2$ (Figure 3A) and an increase in observed molecular mass by MALS, suggesting that the protein forms

a dimer in solution. Using evolving factor analysis (EFA) deconvolution techniques, we separated individual scattering components from the SEC-SAXS curves and derived bead models for these species. A bead model for the no $CaCl_2$ condition corresponds well in shape with the cryo-EM coulomb potential map and it has similar dimensions at ~ 220 x 180 x 75 Å (Figure 3 B), suggesting that the CADH9-GAIN CMM is present in solution.

In the 1 mM $CaCl_2$ condition, the main peak is likely a mixture of a dimer and a monomer due to its MALS molecular weight of 420 kD, which corresponds to roughly 60% dimer (520 kD) and 40 % monomer (260 kD). We used EFA to separate the scattering from the dimer component and build a bead model. The dimer component is extended at ~ 500 x 150 x 100 Å (Figure 3C) and we propose that this extended architecture corresponds to CADH1-8 in an antiparallel configuration (Figure 3D), similar to that reported from atomic force microscopy.[56] One side of the bead model is thinner than the other, in agreement with multiple reports of a hinge region between CADH5 and CADH6.[56,57]

Molecular dynamics simulations support the presence of a hinge region between CADH5-6.

Using the deposited crystal structure of human CELSR1 CADH4-7 (PDB 7SZ8), we investigated the dynamics of the proposed hinge region within the cadherin repeat region of CELSR.[56,57] In CELSR1, two of the canonical acidic calcium coordinating residues between CADH5 and CAHD6 are found as K533 and T564 (Figure 4 A, B). These substitutions prevent the coordination of two out of three Ca^{2+} ions canonically found between cadherin repeats. We ran three simulations (Figure 4C), one with the wild-type CADH4-7 (WT), another where all calcium ions in the CADH5/CADH6 hinge were deleted (ΔCa^{2+}), and a third where the non-canonical calcium coordinating residues were changed to the canonical ones, K533E/T564D, and calcium ions were added manually based on alignments to canonical CADH/CADH interdomain interfaces (Canonical, see Methods). We performed principal component (PC) analysis on the Cα atoms of the three concatenated simulation trajectories and obtained two PCs which capture ~ 87 % of the Cα variance. Following projection onto the PC1-2 subspace, we performed hierarchical clustering (Figure 4C) and examined frames of the simulation

near the centroid of each cluster (Figure 4D). In cluster 1, the molecule is bent to ~ 80 degrees about the CADH5/CADH6 linker region. Cluster 2 is represented by a ~ 45-degree bend in the CADH5/6 linker. Cluster 3 corresponds to an approximately linear configuration. We quantified the fraction of time that each variant spent in each cluster (Figure 4E) and found that while the WT and ΔCa^{2+} simulations can flex about the CADH5/6 hinge and sample both extended and bent conformations, the Canonical simulation is limited to mostly extended conformations.

The cadherin repeat module of CADH1-8 is essential for the adhesive functions of mCELSR1.

To address which portions of mCELSR1 contribute to its adhesive and signaling functions, we split the protein into two modules according to our structural information. We deleted the CADH1-8 module (ΔCADH1-8) as well as the CMM resolved in our structure (ΔCADH9-GAIN) (Figure 5 A and Supplemental Figure S4A, B). We tested the adhesive function of our constructs in cell aggregation assays as well as a cell-cell junction enrichment assay. In the cell aggregation assay, each full-length protein is expressed on two different HEK293T cell populations and a red or green fluorescent reporter is co-expressed. The cells are then mixed, and extent of aggregation is imaged and quantified.[73] WT mCELSR1 was able to efficiently induce aggregation (Figure 5B, C) whereas the ΔCADH1-8 construct was defective in aggregation and the ΔCADH9-GAIN construct was able to form aggregates but not as efficiently as WT. In the cell-cell junction enrichment assay, full length protein is expressed using HEK293T cells observed in groups, and the localization of mCELSR1 is compared to ZO-1, a cell-cell junction marker.[74,75] Similar to the results for the cell aggregation assay, in the cell-cell junction assay, WT mCELSR1 efficiently localized to the cell-cell junction (Figure 5D, E) whereas the ΔCADH1-8 construct was found distributed all over the cell surface, not only at the cell-cell junction. The ΔCADH9-GAIN construct also localized to the cell-cell junction. We report the CADH1-8 module as sufficient for cell-cell adhesion, being that CAHD9 is dispensable for this activity. We also found that WT mCELSR1-mediated aggregation was abolished in the presence of EGTA, a selective Ca^{2+} chelator (Supplemental Figure S4C-E) whereas TEN2/ADGRL3-mediated aggregation was not affected by EGTA, serving as

a control.[59,76] Finally, we found that mCELSR1 and mCELSR2 can form heterophilic aggregates when two cell populations expressing these proteins are mixed (Supplemental Figure S4D, E).

CELSR signaling activity is regulated by the CADH9-GAIN module.

mCELSR1 has previously been shown to couple to $G\alpha_s$ using a BRET2 assay for G protein coupling.[67] This assay measures the dissociation of Gα from Gβɣ which is caused by turnover of Gα into its GTP-bound state by the 7TM (Figure 6A). This manifests as a decrease in BRET2. As seen previously, overexpression of WT mCELSR1 results in lower $G\alpha_s$ BRET2, suggesting that mCELSR1 couples to $G\alpha_s$. We found that the ΔCADH1-8 construct also resulted in lower BRET2, indicating no observable $G\alpha_s$ coupling defect (Figure 6B). The ΔCADH9-GAIN construct did not result in lower BRET2, and thus has a defect in $G\alpha_s$ coupling, suggesting that the CADH9-GAIN module regulates signaling through the 7TM.

Discussion

CELSRs are highly conserved adhesion GPCRs critical for animal development.[4–6] Their large extracellular regions have remained enigmatic; their role in cellular adhesion, signaling, and other functions remain unclear, and molecular-level detail has been sparsely available. In this work, we determined the cryo-EM structure of the mCELSR1 ECR, revealing a CMM containing CADH9-GAIN. We also used functional assays to define two modules of the protein; CADH1-8 is responsible for adhesion and CADH9-GAIN regulates G protein-coupling.

The CADH9-GAIN CMM as an interaction hub with several ligand binding sites

Our work adds a key structure to the landscape of the adhesion GPCRs by defining the three-dimensional structure of the CELSR/ADGRC ECR. The CADH9-GAIN region of mCELSR1 contains 13 domains arranged in a CMM mediated by conserved hydrophobic contacts between the N-terminal CADH9 domain and C-terminal GAIN domain. Our data provide molecular detail to a previous report showcasing low resolution atomic force microscopy images of the full CELSR2 extracellular region.[56] The CADH9-GAIN CMM is large, with a solvent-accessible surface area of 74,000 $Å^2$ and presents

several putative ligand binding sites to the extracellular milieu, including the site on the LamG2 domain. It remains to be defined how the known PCP ligands Frizzled and Van Gogh interact with CELSR1 in cis.[12,77] Additionally, CELSR2 has been shown to dimerize in a parallel configuration via its globular CADH9-GAIN CMM and this binding site remains to be determined.[56] One major limitation of our work is that we did not perform the cryo-EM single particle analysis with added calcium, which is ubiquitous in the extracellular space. Efforts to include $CaCl_2$ in our cryo-EM grids revealed large aggregates of protein which could not be used for single particle analysis. Regardless, our structure is likely valid as the globular region observed using atomic force microscopy in the presence of $CaCl_2$ corresponds well in shape and dimensions to our high-resolution structure of the CADH9-GAIN CMM.[56]

CELSRs dimerize in trans via the CADH1-8 module in an antiparallel fashion similar to protocadherins

Evidence collected by us and others is consistent with a model of the CADH1-8 mediated antiparallel dimer driving the adhesive activity of CELSRs. In the presence of Ca^{2+}, we determined a thin and extended species ~ 500 Å long from our SAXS data which is consistent with an extended antiparallel dimer. This agrees with another report which used atomic force microscopy to determine low resolution images of CELSR ECR constructs.[56] In this model, each protomer is twisted around the other, where CADH1 interacts with CADH8 on the opposing monomer, CADH2 with CADH7, and so forth. This dimerization mode is similar to known protocadherin structures, where the cadherin repeats are arranged in an antiparallel fashion and they twist around each other.[50–55] We propose that this trans antiparallel dimer mediates the adhesive function of CELSR, as our deletion of the CADH1-8 module abrogates cell aggregation activity as well as the cell-cell junction localization of mCELSR1 in cells. The use of EGTA disrupted WT mCELSR1-mediated aggregation, also consistent with a Ca^{2+}-dependent antiparallel dimer of CADH repeats. These data are consistent with what others have found using the cell aggregation assay.[12,13,20] This tight multi-CADH dimer thus may be relevant to the role that CELSRs play in many processes which require the maintenance or coordinated change of cell-cell

contacts in response to changes in force or pressure.[6,8,10,16,17] Future work will reveal the molecular architecture of the CELSR antiparallel dimer, explaining the mechanism of how the known CELSR mutations Crash and Spin Cycle result in neuromuscular dysfunction.[8]

An updated view of adhesion GPCR structure and function: the CMM as a general feature of aGPCRs

We propose that the mCELSR1 CMM is the crucial structural feature which transmits adhesive signals into G protein-coupling (Figure 7). Our results show that the mCELSR1 CMM regulates G protein-coupling as its removal reduces $G\alpha_s$ turnover, and previous work has shown that this $G\alpha_s$ turnover is not affected by the mutation of residues on the tethered agonist which mediate activation in other aGPCRs.[67] Recent work which measured tethered agonist-mediated activation across all adhesion GPCRs shows that while some receptors clearly respond to the tethered agonist, CELSR1 and CELSR3 do not.[78] Taken together, this work suggests that in CELSR1, the CMM can modulate 7TM function independent of the canonical tethered agonist-mediated activation mechanism.

We speculate based on this work that aGPCRs, in general, may have N-terminal regions of their ECRs as adhesive regions and then transmit this adhesion to a C-terminal CMM used for modulating G protein-coupling. Indeed, several aGPCRs employ their N-terminal domains to bind a protein ligand: ADGRL3 with TEN2 and FLRT[59,80–82], ADGRG1 with transglutaminase 2[83], and ADGRG6 with Collagen IV[84]. We add to this list CELSR1 which uses its N-terminal CADH repeats to mediate homophilic adhesion in trans. In each case, the N-terminus extends farthest away from the aGPCR-expressing cell, so it is poised to interact with ligands in the extracellular space. The adhesive 'signal' can then be transferred to a CMM, the simplest version of which is the GAIN domain alone. This adhesive signal could either reveal the tethered agonist in the canonical aGPCR activation mechanism, or the CMM could directly interact with the 7TM to modulate G protein-coupling. Additionally, other aGPCRs have CMMs. ADGRG6 has 5 domains in a CMM mediated by its N-terminal CUB domain.[71] ADGRG1 has an N-terminal PLL domain which is found tightly packed against its GAIN domain, generating a small,

prototypic CMM.[85] In both ADGRG6 and ADGRG1, splice variants can disrupt these CMMs in order to regulate ligand binding and 7TM activity.[71,85,86] The intricate, modular architectures of aGPCRs likely evolved to withstand and react to strict spatial and force requirements in order to mediate intracellular events.[3,7,87–91] More experimental structures of aGPCRs with larger extracellular regions, such as ADGRV1 or ADGRG4, as well as comprehensive mechanistic studies including structural biology, adhesion, and signaling activities, will determine whether the CMM is a general structural feature of adhesion GPCRs.

Materials and Methods

Cloning and construct design

All amino acid numbering in this text is based on *M. musculus* CELSR1, UniProt entry O35161. Bioinformatic tools including PROMALS3D[92], SMART[93], PSIPRED[94] and CDD[95] were used to identify domain boundaries and design CELSR1 constructs. A region containing the mCELSR1 CADH1 through GAIN domains (residues 255-2477) was amplified with these primers: F: 5'-CTGCCTTTGCGGCGAGCACCTCCCCACAGTTCCCCCTGCC-3' and R: 5'-GTGGT GATGGTGATGATGATGATGCTCCCGTCTGCTTATGTC-3' and inserted into the pAcGP67a vector with a C-terminal 8 x histidine tag using Gibson assembly[96].

Cell Culture

Sf9 cells (Thermo Fisher, 12659017) were cultured in SF900-III medium with 10% (v/v) FBS (Sigma-Aldrich, F0926) at 27 °C and transfected with plasmids and commercial baculovirus DNA (Expression Systems, 91-002) using Cellfectin II (Thermo Fisher, 10362100). Following transfection, initial baculoviral stocks were harvested and Sf9 cells were used produce high-titer recombinant baculovirus. As previously described[59]**,** High Five cells (*Trichoplusia ni*, female, ovarian ThermoFisher, B85502) were used for production of recombinant proteins. High Five cells were cultured using Insect-Xpress medium (Lonza, 04351Q) with 10 µg/mL gentamicin at 27 °C. High Five cells (Thermo Fisher, B85502)

were infected with baculovirus at 2.0 x 10^6 cells/mL and incubated at 27 °C with 120 rpm shaking for 72 h.

HEK293T mammalian cells (ATCC, CRL-3216) were used for cell aggregation assays similar to previously described[73] and were cultured in Dulbecco's modified Eagle's medium (DMEM; Gibco, 11965092) supplemented with 10 % FBS (Sigma-Aldrich, F0926) at 37 °C in 5 % CO_2. HEK293T cells (ATCC #CRL-11268) were used for junctional enrichment studies. Cells for junctional enrichment were maintained in DMEM (Gibco Cat# 11995065) plus 10 % FBS (Gibco Cat# 16000044) and 1X Penicillin-Streptomycin (Corning Cat# MT30002CI) at 37 °C and 5 % CO_2 for a maximum of 20 passage numbers. GKO HEK293 cells used for all BRET2 assays were originally a kind gift from Asuka Inoue (Tokyo University, Japan)[97,98]; and were a kind gift from Drs. Vsevolod Gurevich and Chen Zheng (Vanderbilt University). GKO HEK293 cells were maintained in DMEM (Gibco Cat# 11995065) containing 10 % FBS (Gibco Cat# 16000044), 1X Penicillin-Streptomycin (Corning Cat# MT30002CI), and 1x MEM Non-essential Amino Acid (NeA) Solution (Sigma Cat# M7145) at 37 °C and 5 % CO_2.

Protein expression and purification

As previously described[59], media was harvested from High Five cell culture 72 hours after baculovirus infection. The media was centrifuged at room temperature at 900 x g for 15 min. The supernatant was harvested, transferred to a beaker with stirring at room temperature, and the following were added: 50 mM Tris pH 8.0, 5 mM $CaCl_2$ and 1 mM $NiCl_2$ (final concentrations listed). After 30 min, the solution was centrifuged for 30 min at 8000 x g. The clarified supernatant was then incubated with nickel-nitriloacetic (Ni-NTA) resin (QIAGEN 30250) with stirring at room temperature for at least 3 hours. A Büchner funnel was used to collect resin and wash using a buffer composed of 10 mM Tris pH 8.5, 150 mM NaCl (TBS) with 20 mM imidazole, and then the washed resin was transferred to a poly-prep chromatography column (Bio-Rad). The protein was eluted using TBS buffer plus 200 mM imidazole. Fractions containing desired protein were pooled and concentrated using a 100 kDa centrifugal concentrator (Amicon UFC810024) and loaded on gel filtration chromatography using a Superose 6

Increase 10/300 column (GE Healthcare) using the following buffer: 10 mM Tris pH 8.5, 150mM NaCl, with the supplementation of 1 mM $CaCl_2$ as necessary.

SAXS data collection and processing

SAXS was performed at BioCAT (Beamline 18ID at the Advanced Photon Source, Chicago) with in-line size exclusion chromatography (SEC) to separate sample from aggregates and other contaminants thus ensuring optimal sample quality and multiangle light scattering (MALS), dynamic light scattering (DLS) and refractive index measurement (RI) for additional biophysical characterization (SEC-MALS-SAXS). The samples were loaded on a Superose 6 Increase column (Cytiva) run by a 1260 Infinity II HPLC (Agilent Technologies) at 0.6 mL/min. The flow passed through (in order) the Agilent UV detector, a MALS detector and a DLS detector (DAWN Helios II, Wyatt Technologies), and an RI detector (Optilab T-rEX, Wyatt). The flow then went through the SAXS flow cell. The flow cell consists of a 1.0 mm ID quartz capillary with ~20 µm walls. A coflowing buffer sheath is used to separate sample from the capillary walls, helping prevent radiation damage[99]. Scattering intensity was recorded using an Eiger2 XE 9M (Dectris) detector which was placed 3.6 m from the sample giving us access to a q-range of 0.003 $Å^{-1}$ to 0.42 $Å^{-1}$. 0.5 s exposures were acquired every 1 s during elution and data were reduced using BioXTAS RAW 2.1.4[100]. Buffer blanks were created by averaging regions flanking the elution peak and the entire series was buffer subtracted. The buffer subtracted series was analyzed using evolving factor analysis within RAW and separated into individual scattering components and the separated I(q) vs q curves were used for subsequent analyses. The GNOM and DAMMIF/N packages within RAW were used to calculate IFTs and bead models for each scattering component. Molecular weights and hydrodynamic radii were calculated from the MALS and DLS data respectively using the ASTRA 7 software (Wyatt).

Cryo-EM data collection

3.5 µL purified mCELSR1 CADH1-GAIN (3.0 mg/mL) was applied on glow-discharged holey carbon grids (Quantifoil R1.2/1.3, 300 mesh), and vitrified using a Vitrobot Mark IV (FEI Company). The

specimen was visualized at the National Cryo-EM Facility using a Titan Krios electron microscope (FEI) operating at 300 kV and equipped with a K3 direct electron detector (Gatan, Inc.) with the Latitude software (Gatan, Inc.). Images were recorded with a nominal magnification of ×81,000 in super-resolution counting mode, corresponding to a pixel size of 0.55 Å on the specimen level. To maximize data collection speed while keeping image aberrations minimal, image shift was used as imaging strategy using one data position per hole with six holes targeted in one template with one focus position. In total, 5826 images with defocus values in the range of −1.0 to −2.0 µm were recorded using a dose rate of 6.2 electrons/s/physical pixel. The total exposure time was set to 2.5 s resulting in an accumulated dose of about 50 electrons per $Å^2$ and a total of 50 frames per movie stack. In order to improve resolution, a second dataset of 5550 micrographs was collected in exactly the same manner on the same microscope and the two particle stacks were combined at the stage of 3D classification.

Cryo-EM processing and model building

RELION 4.0 was used for the initial steps of data processing on each set of micrographs separately[101]. Stack images were subjected to beam-induced motion correction using MotionCor2 and binned to 1.1 Å/pixel.[102] CTF parameters for each micrograph were determined by CTFFIND4.[103] In total, ~1.8 million particle projections were selected from each dataset using TOPAZ[104] automated particle picking and subjected to reference-free two-dimensional classification to discard particles categorized in poorly defined classes. The initial 3D maximum-likelihood-based classification was performed using an AlphaFold2[72] generated model of CADH9-GAIN as the reference model, low-pass filtered to 40 Å. This model was not used after the initial 3D classification. After successive rounds of 3D classification, ~ 500K particles from each dataset, ~ 1 million particles total, were subjected to the 3D initial model job type with three classes to ensure that the AlphaFold2 model did not bias the later processing steps. The 1 million particles and the best 3D volume were selected and imported into CryoSPARC 4.1.2. These particles were subjected to iterative rounds of heterogeneous refinement with 3 classes (best one imported from Relion 3D Initial Model, and two junk classes) until resolution did not improve any

further. Final particle number in the best class was 171,416. Non-uniform refinement using the particles from the best class was used to obtain the final map, which was sharpened using local filtering in cryoSPARC for display in the manuscript and for manual model building. The detailed data processing flow is shown in Supplementary Fig. S2. Reported resolutions are based on the gold-standard Fourier shell correlation (FSC) using the 0.143 criterion. Model building started from the AlphaFold2 model of CADH9-GAIN, which was docked into the EM density map using Phenix, refined using the real-space refinement module in the Phenix software suite[105] and then manually checked and adjusted residue-by-residue to fit the density using COOT[106]. The final model and map were input to the real-space refinement module in the Phenix software suite before deposition[105].

Structural analysis and sequence conservation analysis

Structural analysis and manual inspection of structures was performed using PyMOL version 2.4.1 (Schrodinger) and sequence analysis was done using PROMALS3D[92] and the ConSurf[107] server. ChimeraX was used to analyze cryo-EM density maps and generate figures[108].

Molecular dynamics simulations

The structure used for these simulations was previously solved by Tamilselvan and Sotomayor (PDB ID 7SZ8).[57] Atoms missing from the crystal structure were added with Swiss PDB Viewer. Crystal structure waters and sodium ions were removed from the protein. Using GROMACS version 2022.1, CELSR1 CADH4-7 was placed in a 8216.1 nm^3 rhombal dodecahedron with side length 13.9 nm and periodic boundary conditions, ensuring over 1 nm of solvent between the most distant atoms of 7SZ8 and the boundaries. The box was solvated with the TIP3P water model using gmx solvate and Na^+ and Cl^- counterions were added using gmx genion. The protein's structure was minimized with the leapfrog integrator in step sizes of 0.1 Å until the max force was smaller than 1000 kJ mol^{-1} nm^{-1}.

The system was then subjected to a two-phase equilibration in the NVT and NPT ensembles with protein atoms under harmonic position restraints. A 100ps NVT equilibration was carried out with step size 2 fs at 300 K with the Berendsen thermostat using a 0.1 ps coupling constant, and solvent velocities

were assigned from the Boltzmann distribution. NPT equilibration was also carried out with step size 2 fs for 100ps, and at 1 atm with Parrinello-Rahman pressure coupling (2.0 ps coupling constant) using velocities from NVT ensemble. Simulations on the unrestrainted protein were run in the NPT ensemble for 1 μs and a 2 fs step size. Long-range electrostatics were computed with PME with a 1.6 A° Fourier spacing and 10 A° cutoff. All simulations were run with the AMBER99SB-ILDN force field. Different simulation conditions were separately solvated, minimized, and equilibrated as above.

Simulated systems

Condition	Simulation Length
WT	100 ns
K533E/T564D	100 ns
ΔCa^{2+}	100 ns

The WT simulation was prepared as described above. The K533/T564 simulation was designed by aligning calcium coordinating junctions (CADH 4-5 and CADH 6-7) to the CADH 5-6 junction. After alignment, K533E and T564D were changed to match the calcium coordination geometry of the canonical sites, and the two missing calcium ions were added into their respective positions to make a three-calcium interdomain junction between cadherins 5 and 6. The ΔCa^{2+} simulation was prepared by removing the calcium ion between CADH 5 and 6 from the WT protein.

PCA and free energy landscape analysis

Trajectories from the simulations were extracted for the alpha carbons (Cαs) of each residue for each simulation. Principal components of the Cαs were calculated by concatenating all three simulation trajectories for each with gmx trjcat and diagonalizing the covariate matrix with gmx covar. Trajectories were projected onto essential gmx anaeig and were plotted and visualized with a homemade python script. The fractions of variance f captured by PCs were checked to verify that the first two principal

components captured most of the variance and verify the quality of the dimension reduction by computing

$$f = \frac{\{\lambda_i\}_{1 \le i \le 3N}}{\mathrm{tr}(C)}$$

where $\{\lambda_i\}_{1 \le i \le 3N}$ is the set of $3N$ eigenvalues for N α-carbons, and $\mathrm{tr}(C)$ is the trace of the covariate matrix. Hierarchical clustering of free energy landscape wells was performed by scipy.cluster in a homemade python script using the Ward clustering method to minimize variance in the l^2 norm. Cluster centroids c_i were computed by averaging the PC1 and PC2 coordinates of frames within each cluster

$$c_i = \frac{1}{N_i} \sum_{j \in \text{ cluster } i} (\text{PC1,PC2})_j$$

where N_i is the number of frames in the ith cluster. We chose the frame from the simulations whose PC coordinates are closest by l^2 norm and constructed the 3D structure as a linear combination of PC1 and PC2 using gmx anaeig.

Cell aggregation assay

As previously described[73], HEK293T cells (ATCC, CRL-3216) were seeded using a 6-well plate in 2 mL of DMEM supplemented with 10% FBS and incubated overnight at 37 °C. When the cells reached ~ 60 % confluency, they were co-transfected with 1 μg each of either pCMV5 + GFP or dsRed, CELSR1 + GFP or dsRed, CELSR2 + GFP or dsRed, ADGRL3 + GFP and TEN2 + dsRed and 5 µL LipoD293T (SL100668; SignaGen Laboratories). Two days after transfection, the media was aspirated and the cells were washed with 1xPBS, detached with 1xPBS containing 1 mM EGTA, and supplemented with 15 μL of 50 mg ml−1 DNAse IV (Sigma, D5025). The cells were resuspended by pipetting to a create single-cell suspensions, transferred to a microcentrifuge tube and an additional 15 μL of DNAse solution was added to each sample. Seventy μL of cells expressing the indicated constructs were mixed in a 1:1 ratio in one well of a non-coated 24-well plate containing 360 μL of DMEM supplemented with 10 % FBS, 20 mM $CaCl_2$ and 10 mM $MgCl_2$ or DMEM with 10 % FBS, 10 mM $MgCl_2$, and 20 mM EGTA for 5 hours at 126 rpm at 37 °C with 5% CO2 and imaged using a Leica Fluorescence Microscope with

a 5× objective. Aggregation index at time = 5 hrs was calculated using ImageJ 1.52e. A value for particle area of 2-3 cells was set as a threshold based on negative control values. The aggregation index was calculated by dividing the area of particles exceeding this threshold by the total area occupied by all particles in the individual fields.

Immunocytochemistry

Cover glass (#0, 12 mm, Carolina Biological Supply Company #633009) was placed into 24-well plates and coated for 2 hrs with 100 μL of 50 μg/mL poly-D-lysine (Gibco #A38904-01) in the 37 °C tissue culture incubator. Excess poly-D-lysine was removed, coverslips were washed 3x with sterile ddH_2O, and dried for 30 mins. HEK293T cells were plated at 1.5 x 10^5 cells/well in 0.5 mL complete DMEM. After 16-24 hrs, cells were transfected with indicated experimental plasmid via TransIT-2020 (Mirus MIR5400) with a total of 0.5 μg DNA amount/condition/well. After 48 hrs post-transfection, cells were washed briefly once with PBS, fixed with 4 % PFA (Electron Microscopy Science Cat# 15714) with 4% sucrose in PBS for 20 min at 4 ºC, and washed 3 x 5 mins in PBS. For surface receptor labeling of HA tag, samples were then transferred directly into blocking buffer (4 % BSA (Sigma Cat# 10735086001) plus 3 % normal goat serum (Jackson Immunoresearch #005000121) in PBS) for 1 hr. Samples were then labeled with HA tag primary antibody (anti-HA mouse, Covance Cat# MMS101R; 1:2,000) diluted into blocking buffer for 2 hrs at room temperature. Samples were washed 3 x 5 mins with PBS, permeabilized with 0.2% Triton X-100 in PBS for 5 mins at room temperature and incubated in primary ZO-1 antibody (ZO-1 polyclonal rabbit antibody, Invitrogen #61-7300, 1:2,000) diluted into blocking buffer for 2 hrs at room temperature. Samples were subsequently washed 3 x 5 mins with PBS and incubated in fluorescently conjugated secondary antibodies (goat anti-mouse Alexa Fluor 488, ThermoFisher #A11001, 1:1,000; goat anti-rabbit Alexa Fluor 546, ThermoFisher #A11010, 1:1,000) diluted into blocking buffer together with Phalloidin Alexa 647 (ThermoFisher #A22287, 1:40 in methanol) for 30 mins at room temperature. Samples were then washed three times in PBS and

mounted on UltraClear microscope slides (Denville Scientific Cat# M1021) using 10 μL ProLong Gold antifade reagent (Invitrogen, #P36930) per coverslip.

Fluorescence microscopy

Images were acquired using a Nikon A1r resonant scanning Eclipse Ti2 HD25 confocal microscope with a 10x (Nikon #MRD00105, CFI60 Plan Apochromat Lambda, N.A. 0.45), 20x (Nikon #MRD00205, CFI60 Plan Apochromat Lambda, N.A. 0.75), and 60x (Nikon #MRD01605, CFI60 Plan Apochromat Lambda, N.A. 1.4) objectives, operated by NIS-Elements AR v4.5 acquisition software. Laser intensities and acquisition settings were established for individual channels and applied to entire experiments. Junctional enrichment assay images were collected at 0.07 μm/pixel resolution with 0.07 μm z-step sizes, denoised, and deconvoluted with Richardson-Lucy 3D deconvolution. Image analysis was conducted with Nikon Elements. For the Junction Enrichment analysis, junction enrichment was calculated as a ratio between the corrected mean intensity at junctions (indicated by ZO-1) and the corrected total intensity of the cells in contact. Corrected mean intensities at the regions of interests were obtained by background subtracting mean intensities of the empty vector condition.

BRET2 G protein-coupling Assay

HEK G-protein K.O cells[98] were plated into 12-well plate at a density of 3-4 x 10^5 cells in 1 mL per well. HEK G.K.O. media contained 1x DMEM (Gibco Cat# 11995065) plus 10 % FBS (Gibco Cat#16000044), 1X Penicillin-Streptomycin (Corning Cat#MT30002CI) with 1x MEM Non-essential Amino Acid (NeA) Solution (Sigma Cat# M7145). After 16-24 hours, cells were co-transfected with increasing amounts of mCELSR1 receptor, WT or mutants (1, 2, 4, 6, and 8 μg), and TRUPATH plasmids at 1:1:1 DNA ratio (Gα-RLuc8:Gβ:Gγ-GFP2) via TransIT-2020 (Mirus Cat# MIR5400). Each condition required 97 μL of room-temperature 1x Opti-MEM (Gibco Cat# 31985070), 1 μL each DNA TRUPAPH plasmid at 1μg/μL concentration), 8 μL of 1μg/μL of the receptor plasmid/empty vector, and 3 μL of room-temperature and gently vortexed TransIT-2020 reagent. The volume of the reactions was maintained consistent with an addition of empty vector. The TransIT-2020:DNA complexes were gently mixed via pipetting 10 times

and incubated at room temperature for 20 mins before dropwise addition into the well. The plate was rocked gently side to side and incubated at 37 ºC 24 hours before harvesting. In each well, media was aspirated, and cells were washed with 1 mL warm PBS. Cells were detached with 300 μL warm Versene (Gibco Cat# 15040066) and incubated at 37 ºC for 5 mins then resuspended via pipetting 10 times. Cells were plated in 200 μL complete DMEM containing 1x NeA at a density of 30,000–50,000 cells per well in Matrigel-coated 96-well assay plate. Each experimental condition was plated into three separate wells within the 96-well assay plate. BRET2 assays were performed 48 hours after transfection. In each well, media was aspirated, and cells were incubated in 90 μL of 1x Hanks' balanced Salt Solution (Gibco Cat# 14175095) with 20 mM HEPES (Sigma Cat# H3375, pH 7.4) and 10 μL 100 μM Coelenterazine-400a (NanoLight Technologies Cat# 340) diluted in PBS for 5 minutes. BRET intensities were measured via BERTHOLD TriStar2 LB 942 Multimode Reader with Deep Blue C filter (410nm) and GFP2 filter (515 nm). The BRET ratio was obtained by calculating the ratio of GFP2 signal to Deep Blue C signal per well. The BRET2 ratio of the three wells per condition were then averaged. Net BRET2 was subsequently calculated by subtracting the BRET2 ratio of cells expressing donor only (Gα-RLuc8) from the BRET2 ratio of each respective experimental condition.

Statistical Analysis

All statistical analysis was performed using Graphpad Prism 10. For the cell aggregation assays, cell-cell junction assays, and BRET2 assays, all experiments were performed in at least N=3 independent experiments in at least triplicate. For the cell aggregation assays and cell-cell junction assays, the one-way ANOVA with Dunnett's post hoc correction for multiple comparisons was used to assess statistical significance. For the BRET2 assays, a two-way ANOVA with Tukey's post hoc correction for multiple comparisons was used to assess statistical significance.

References

1. Hamann, J. *et al.* International union of basic and clinical pharmacology. XCIV. adhesion G protein-coupled receptors. *Pharmacol. Rev.* **67**, 338–367 (2015).
2. Purcell, R. H. & Hall, R. A. Annual Review of Pharmacology and Toxicology Adhesion G Protein-Coupled Receptors as Drug Targets. (2017) doi:10.1146/annurev-pharmtox.
3. Araç, D. & Leon, K. Structure, function and therapeutic potential of adhesion GPCRs. *GPCRs Struct. Funct. Drug Discov.* 23–41 (2019) doi:10.1016/B978-0-12-816228-6.00002-7.
4. Boutin, C., Goffinet, A. M. & Tissir, F. Celsr1-3 Cadherins in PCP and Brain Development. in *Current Topics in Developmental Biology* vol. 101 161–183 (Academic Press Inc., 2012).
5. Tissir, F. & Goffinet, A. M. Atypical cadherins Celsr1-3 and planar cell polarity in vertebrates. in *Progress in Molecular Biology and Translational Science* vol. 116 193–214 (Elsevier B.V., 2013).
6. Wang, X. J. *et al.* Understanding cadherin EGF LAG seven-pass G-type receptors. *J. Neurochem.* **131**, 699–711 (2014).
7. Langenhan, T., Piao, X. & Monk, K. R. Adhesion G protein-coupled receptors in nervous system development and disease. *Nat. Rev. Neurosci.* **17**, 550–561 (2016).
8. Curtin, J. A. *et al.* Mutation of Celsr1 Disrupts Planar Polarity of Inner Ear Hair Cells and Causes Severe Neural Tube Defects in the Mouse involvement of a planar cell polarity pathway in vertebrate neurulation. *Curr. Biol.* **13**, 1129–1133 (2003).
9. Shi, D. *et al.* Celsr1 is required for the generation of polarity at multiple levels of the mouse oviduct. *Dev.* **141**, 4558–4568 (2014).
10. Duncan, J. S. *et al.* Celsr1 coordinates the planar polarity of vestibular hair cells during inner ear development. *Dev. Biol.* **423**, 126–137 (2017).
11. Devenport, D. & Fuchs, E. Planar polarization in embryonic epidermis orchestrates global asymmetric morphogenesis of hair follicles. *Nat. Cell Biol.* **10**, 1257–1268 (2008).
12. Stahley, S. N., Basta, L. P., Sharan, R. & Devenport, D. Celsr1 adhesive interactions mediate the asymmetric organization of planar polarity complexes. *Elife* **10**, 1–26 (2021).
13. Usui Tadao *et al.* Flamingo, a seven-pass transmembrane cadherin, regulates planar cell polarity under the control of Frizzled. *Cell* **98**, 585–595 (1999).
14. Nishimura, T., Honda, H. & Takeichi, M. Planar cell polarity links axes of spatial dynamics in neural-tube closure. *Cell* **149**, 1084–1097 (2012).
15. Ravni, A., Qu, Y., Goffinet, A. M. & Tissir, F. Planar cell polarity cadherin Celsr1 regulates skin hair patterning in the mouse. *Journal of Investigative Dermatology* vol. 129 2507–2509 (2009).
16. Tissir, F. *et al.* Lack of cadherins Celsr2 and Celsr3 impairs ependymal ciliogenesis, leading to fatal hydrocephalus. *Nat. Neurosci.* **13**, 700–707 (2010).
17. Tatin, F. *et al.* Planar cell polarity protein Celsr1 regulates endothelial adherens junctions and directed cell rearrangements during valve morphogenesis. *Dev. Cell* **26**, 31–44 (2013).
18. Tissir, F., Bar, I., Jossin, Y. & Goffinet, A. M. Protocadherin Celsr3 is crucial in axonal tract development. *Nat. Neurosci.* **8**, 451–457 (2005).
19. Zhou, L., Tissir, F. & Goffinet, A. M. The Atypical Cadherin Celsr3 Regulates the Development of the Axonal Blueprint. in *Cortical Development: Genes and Genetic Abnormalities* 130–134 (John Wiley and Sons Ltd., 2008). doi:10.1002/9780470994030.ch10.
20. Shima, Y., Kengaku, M., Hirano, T., Takeichi, M. & Uemura, T. *Regulation of Dendritic Maintenance and Growth by a Mammalian 7-Pass Transmembrane Cadherin*. *Developmental Cell* vol. 7 http://www.developmentalcell. (2004).
21. Qu, Y. *et al.* Atypical cadherins Celsr1-3 differentially regulate migration of facial branchiomotor neurons in mice. *J. Neurosci.* **30**, 9392–9401 (2010).
22. Glasco, D. M. *et al.* The atypical cadherin Celsr1 functions non-cell autonomously to block rostral migration of facial branchiomotor neurons in mice. *Dev. Biol.* **417**, 40–49 (2016).

23. Formstone, C. J. & Little, P. F. R. The flamingo-related mouse Celsr family (Celsr1–3) genes exhibit distinct patterns of expression during embryonic development. *Mech. Dev.* **109**, 91–94 (2001).
24. Tissir, F., De-Backer, O., Goffinet, A. M. & Lambert de Rouvroit, C. Developmental expression profiles of Celsr (Flamingo) genes in the mouse. *Mech. Dev.* **112**, 157–160 (2002).
25. Shima, Y. *et al.* Differential expression of the seven-pass transmembrane cadherin genes Celsr1-3 and distribution of the Celsr2 protein during mouse development. *Dev. Dyn.* **223**, 321–332 (2002).
26. Formstone, C. J., Moxon, C., Murdoch, J., Little, P. & Mason, I. Basal enrichment within neuroepithelia suggests novel function(s) for Celsr1 protein. *Mol. Cell. Neurosci.* **44**, 210–222 (2010).
27. Chen, Z. *et al.* Genetic analysis of Wnt/PCP genes in neural tube defects. *BMC Med. Genomics* **11**, (2018).
28. Qiao, X. *et al.* Genetic analysis of rare coding mutations of CELSR1-3 in congenital heart and neural tube defects in Chinese people. *Clin. Sci.* **130**, 2329–2340 (2016).
29. Allache, R., De Marco, P., Merello, E., Capra, V. & Kibar, Z. Role of the planar cell polarity gene CELSR1 in neural tube defects and caudal agenesis. *Birth Defects Res. Part A - Clin. Mol. Teratol.* **94**, 176–181 (2012).
30. Robinson, A. *et al.* Mutations in the planar cell polarity genes CELSR1 and SCRIB are associated with the severe neural tube defect craniorachischisis. *Hum. Mutat.* **33**, 440–447 (2012).
31. Lei, Y. *et al.* Identification of novel CELSR1 mutations in spina bifida. *PLoS One* **9**, (2014).
32. Maltese, P. E. *et al.* Increasing evidence of hereditary lymphedema caused by CELSR1 loss-of-function variants. *Am. J. Med. Genet. Part A* **179**, 1718–1724 (2019).
33. Smith, M. S., Sarasua, S. M., Rogers, C., Phelan, K. & Boccuto, L. Lymphedema is associated with CELSR1 in Phelan–McDermid syndrome. *Clin. Genet.* (2023) doi:10.1111/cge.14364.
34. Sudduth, C. L. *et al.* Primary Upper Extremity Lymphedema Caused by a CELSR1 Variant. *J. Vasc. Anomalies* **3**, e041 (2022).
35. Gonzalez-Garay, M. L. *et al.* A novel mutation in CELSR1 is associated with hereditary lymphedema. *Vasc. Cell* **8**, (2016).
36. Seo, S. H. *et al.* Clinical staging and genetic profiling of Korean patients with primary lymphedema using targeted gene sequencing. *Sci. Rep.* **12**, (2022).
37. Kaucká, M. *et al.* The planar cell polarity pathway drives pathogenesis of chronic lymphocytic leukemia by the regulation of b-lymphocyte migration. *Cancer Res.* **73**, 1491–1501 (2013).
38. Vilboux, T. *et al.* CELSR2, encoding a planar cell polarity protein, is a putative gene in Joubert syndrome with cortical heterotopia, microophthalmia, and growth hormone deficiency. *Am. J. Med. Genet. Part A* **173**, 661–666 (2017).
39. Shaheen, R. *et al.* Characterizing the morbid genome of ciliopathies. *Genome Biol.* **17**, 1–11 (2016).
40. Willsey, A. J. *et al.* De Novo Coding Variants Are Strongly Associated with Tourette Disorder. *Neuron* **94**, 486-499.e9 (2017).
41. Hulpiau, P. & Van Roy, F. New insights into the evolution of metazoan cadherins. *Mol. Biol. Evol.* **28**, 647–657 (2011).
42. Berger-Müller, S. & Suzuki, T. Seven-pass transmembrane cadherins: roles and emerging mechanisms in axonal and dendritic patterning. *Mol. Neurobiol.* **44**, 313–320 (2011).
43. Gul, I. S., Hulpiau, P., Saeys, Y. & van Roy, F. Evolution and diversity of cadherins and catenins. *Experimental Cell Research* vol. 358 3–9 (2017).
44. Shapiro, L. & Weis, W. I. Structure and biochemistry of cadherins and catenins. *Cold Spring Harb. Perspect. Biol.* **1**, 1–21 (2009).
45. Honig, B. & Shapiro, L. Adhesion Protein Structure, Molecular Affinities, and Principles of Cell-

Cell Recognition. *Cell* **181**, 520–535 (2020).
46. Leckband, D. E. & de Rooij, J. Cadherin adhesion and mechanotransduction. *Annu. Rev. Cell Dev. Biol.* **30**, 291–315 (2014).
47. De-la-Torre, P., Choudhary, D., Araya-Secchi, R., Narui, Y. & Sotomayor, M. A Mechanically Weak Extracellular Membrane-Adjacent Domain Induces Dimerization of Protocadherin-15. *Biophys. J.* **115**, 2368–2385 (2018).
48. Hulpiau, P. & van Roy, F. Molecular evolution of the cadherin superfamily. *International Journal of Biochemistry and Cell Biology* vol. 41 349–369 (2009).
49. Tanoue, T. & Takeichi, M. New insights into fat cadherins. *J. Cell Sci.* **118**, 2347–2353 (2005).
50. Goodman, K. M. *et al.* Structural Basis of Diverse Homophilic Recognition by Clustered α- and β-Protocadherins. *Neuron* **90**, 709–723 (2016).
51. Brasch, J. *et al.* Visualization of clustered protocadherin neuronal self-recognition complexes. *Nature* **569**, 280–283 (2019).
52. Harrison, O. J. *et al.* Family-wide Structural and Biophysical Analysis of Binding Interactions among Non-clustered δ-Protocadherins. *Cell Rep.* **30**, 2655-2671.e7 (2020).
53. Sotomayor, M., Weihofen, W. A., Weihofen, W. A. & Corey, D. P. Structure of a force-conveying cadherin bond essential for inner-ear mechanotransduction. *Nature* **492**, 128–132 (2012).
54. Rubinstein, R. *et al.* Molecular Logic of Neuronal Self-Recognition through Protocadherin Domain Interactions. *Cell* **163**, 629–642 (2015).
55. Jaiganesh, A., Narui, Y., Araya-Secchi, R. & Sotomayor, M. Beyond cell–cell adhesion: Sensational cadherins for hearing and balance. *Cold Spring Harb. Perspect. Biol.* **10**, (2018).
56. Nishiguchi, S., Kasai, R. S. & Uchihashi, T. Antiparallel dimer structure of CELSR cadherin in solution revealed by high-speed-atomic force microscopy. *Proc. Natl. Acad. Sci. U. S. A.* **120**, (2023).
57. Tamilselvan, E. & Sotomayor, M. CELSR1, a core planar cell polarity protein, features a weakly adhesive and flexible cadherin ectodomain. *Structure* **32**, 1–16 (2024).
58. Li, J. *et al.* Structural Basis for Teneurin Function in Circuit-Wiring: A Toxin Motif at the Synapse. *Cell* **173**, 735-748.e15 (2018).
59. Li, J. *et al.* Alternative splicing controls teneurin-latrophilin interaction and synapse specificity by a shape-shifting mechanism. *Nat. Commun.* **11**, 2140 (2020).
60. Meijer, D. H., Frias, C. P., Beugelink, J. W., Deurloo, Y. N. & Janssen, B. J. C. Teneurin4 dimer structures reveal a calcium-stabilized compact conformation supporting homomeric trans-interactions. *EMBO J.* **41**, 1–18 (2022).
61. Pavšič, M., Gunčar, G., Djinovi-Carugo, K. & Lenarčič, B. Crystal structure and its bearing towards an understanding of key biological functions of EpCAM. *Nat. Commun.* **5**, (2014).
62. Chen, F., Venugopal, V., Murray, B. & Rudenko, G. The structure of neurexin 1α reveals features promoting a role as synaptic organizer. *Structure* **19**, 779–789 (2011).
63. Gogou, C. *et al.* Alternative splicing controls teneurin-3 compact dimer formation for neuronal recognition. *bioRxiv* 1–34 (2023).
64. Yamagata, A. *et al.* Structural insights into modulation and selectivity of transsynaptic neurexin–LRRTM interaction. *Nat. Commun.* **9**, 1–11 (2018).
65. Araç, D. *et al.* Structures of Neuroligin-1 and the Neuroligin-1/Neurexin-1β Complex Reveal Specific Protein-Protein and Protein-Ca2+ Interactions. *Neuron* **56**, 992–1003 (2007).
66. Araç, D. *et al.* A novel evolutionarily conserved domain of cell-adhesion GPCRs mediates autoproteolysis. *EMBO J.* **31**, 1364–1378 (2012).
67. Bui, D. L. H. *et al.* The adhesion GPCRs CELSR1–3 and LPHN3 engage G proteins via distinct activation mechanisms. *Cell Rep.* **42**, (2023).
68. Read, J. *From Alchemy to Chemistry*. (Courier Corporation, 1995, 1995).
69. Chug, H., Trakhanov, S., Hülsmann, B. B., Pleiner, T. & Görlich, D. Crystal structure of the

metazoan Nup62•Nup58•Nup54 nucleoporin complex. *Science (80-.).* **350**, 106–110 (2015).
70. Holm, L., Laiho, A., Törönen, P. & Salgado, M. DALI shines a light on remote homologs: One hundred discoveries. *Protein Sci.* **32**, 1–18 (2023).
71. Leon, K. *et al.* Structural basis for adhesion G protein-coupled receptor Gpr126 function. *Nat. Commun.* **11**, (2020).
72. Mirdita, M. *et al.* ColabFold: making protein folding accessible to all. *Nat. Methods* **19**, 679–682 (2022).
73. Kordon, S. P. *et al.* Isoform- and ligand-specific modulation of the adhesion GPCR ADGRL3/Latrophilin3 by a synthetic binder. *Nat. Commun.* **14**, (2023).
74. Inada, M., Izawa, G., Kobayashi, W. & Ozawa, M. 293 Cells Express Both Epithelial As Well As Mesenchymal Cell Adhesion Molecules. *Int. J. Mol. Med.* **37**, 1521–1527 (2016).
75. Beutel, O., Maraspini, R., Pombo-García, K., Martin-Lemaitre, C. & Honigmann, A. Phase Separation of Zonula Occludens Proteins Drives Formation of Tight Junctions. *Cell* **179**, 923-936.e11 (2019).
76. del Toro, D. *et al.* Structural Basis of Teneurin-Latrophilin Interaction in Repulsive Guidance of Migrating Neurons. *Cell* **180**, 323-339.e19 (2020).
77. Basta, L. P. *et al.* Celsr1 and Celsr2 exhibit distinct adhesive interactions and contributions to planar cell polarity. *Front. Cell Dev. Biol.* **10**, (2023).
78. Dates, A. N. *et al.* Heterogeneity of Tethered Agonist Signaling in Adhesion G Protein-Coupled Receptors. *bioRxiv* (2023) doi:https://doi.org/10.1101/2022.07.14.500097.
79. Strutt, H. *et al.* Article Molecular symmetry breaking in the Frizzled- dependent planar polarity pathway Molecular symmetry breaking in the Frizzled-dependent planar polarity pathway. *Curr. Biol.* 1–15 (2023) doi:10.1016/j.cub.2023.10.071.
80. Lu, Y. C. *et al.* Structural Basis of Latrophilin-FLRT-UNC5 Interaction in Cell Adhesion. *Structure* **23**, 1678–1691 (2015).
81. del Toro, D. *et al.* Structural Basis of Teneurin-Latrophilin Interaction in Repulsive Guidance of Migrating Neurons. *Cell* **180**, 323-339.e19 (2020).
82. Jackson, V. A. *et al.* Structural basis of latrophilin-FLRT interaction. *Structure* **23**, 774–781 (2015).
83. Salzman, G. S., Zhang, S., Fernandez, C. G., Araç, D. & Koide, S. Specific and direct modulation of the interaction between adhesion GPCR GPR56/ADGRG1 and tissue transglutaminase 2 using synthetic ligands. *Sci. Rep.* **10**, 1–9 (2020).
84. Paavola, K. J., Sidik, H., Zuchero, J. B., Eckart, M. & Talbot, W. S. Type IV collagen is an activating ligand for the adhesion G protein-coupled receptor GPR126. *Sci. Signal.* **7**, 1–10 (2014).
85. Salzman, G. S. *et al.* Structural Basis for Regulation of GPR56/ADGRG1 by Its Alternatively Spliced Extracellular Domains. *Neuron* **91**, 1292–1304 (2016).
86. Li, T. *et al.* A splicing isoform of GPR56 mediates microglial synaptic refinement via phosphatidylserine binding. *EMBO J.* **39**, 1–20 (2020).
87. Vizurraga, A., Adhikari, R., Yeung, J., Yu, M. & Tall, G. G. Mechanisms of Adhesion G protein Coupled Receptor Activation. *J. Biol. Chem.* jbc.REV120.007423 (2020) doi:10.1074/jbc.rev120.007423.
88. Wilde, C., Mitgau, J., Suchý, T., Schöneberg, T. & Liebscher, I. Translating the force—mechano-sensing GPCRs. *Am. J. Physiol. - Cell Physiol.* **322**, C1047–C1060 (2022).
89. Fu, C. *et al.* Unveiling Mechanical Activation: GAIN Domain Unfolding and Dissociation in Adhesion GPCRs. *Nano Lett.* **23**, 9179–9186 (2023).
90. Zhong, B. L. *et al.* Piconewton Forces Mediate GAIN Domain Dissociation of the Latrophilin-3 Adhesion GPCR. *Nano Lett.* **23**, 9187–9194 (2023).
91. Mitgau, J. *et al.* The N Terminus of Adhesion G Protein–Coupled Receptor GPR126/ADGRG6

as Allosteric Force Integrator. *Front. Cell Dev. Biol.* **10**, 1–13 (2022).
92. Pei, J., Kim, B. H. & Grishin, N. V. PROMALS3D: A tool for multiple protein sequence and structure alignments. *Nucleic Acids Res.* **36**, 2295–2300 (2008).
93. Letunic, I., Khedkar, S. & Bork, P. SMART: Recent updates, new developments and status in 2020. *Nucleic Acids Res.* **49**, D458–D460 (2021).
94. Buchan, D. W. A. & Jones, D. T. The PSIPRED Protein Analysis Workbench: 20 years on. *Nucleic Acids Res.* **47**, W402–W407 (2019).
95. Wang, J. *et al.* The conserved domain database in 2023. *Nucleic Acids Res.* **51**, D384–D388 (2023).
96. Gibson, D. G. *et al.* Enzymatic assembly of DNA molecules up to several hundred kilobases. *Nat. Methods* **6**, 343–345 (2009).
97. Alvarez-Curto, E. *et al.* Targeted elimination of G proteins and arrestins defines their specific contributions to both intensity and duration of G protein-coupled receptor signaling. *J. Biol. Chem.* **291**, 27147–27159 (2016).
98. Grundmann, M. *et al.* Lack of beta-arrestin signaling in the absence of active G proteins. *Nat. Commun.* **9**, 1–7 (2018).
99. Kirby, N. *et al.* Improved radiation dose efficiency in solution SAXS using a sheath flow sample environment. *Acta Crystallogr. Sect. D Struct. Biol.* **72**, 1254–1266 (2016).
100. Hopkins, J. B., Gillilan, R. E. & Skou, S. BioXTAS RAW: Improvements to a free open-source program for small-angle X-ray scattering data reduction and analysis. *J. Appl. Crystallogr.* **50**, 1545–1553 (2017).
101. Kimanius, D., Dong, L., Sharov, G., Nakane, T. & Scheres, S. H. W. New tools for automated cryo-EM single-particle analysis in RELION-4.0. *Biochem. J.* **478**, 4169–4185 (2021).
102. Zheng, S. Q. *et al.* MotionCor2: anisotropic correction of beam-induced motion for improved cryo-electron microscopy. *Nat. Methods* **14**, 331–332 (2017).
103. Rohou, A. & Grigorieff, N. CTFFIND4: Fast and accurate defocus estimation from electron micrographs. *J. Struct. Biol.* **192**, 216–221 (2015).
104. Bepler, T. *et al.* Positive-unlabeled convolutional neural networks for particle picking in cryo-electron micrographs. *Nat. Methods* **16**, 1153–1160 (2019).
105. Liebschner, D. *et al.* Macromolecular structure determination using X-rays, neutrons and electrons: Recent developments in Phenix. *Acta Crystallogr. Sect. D Struct. Biol.* **75**, 861–877 (2019).
106. Emsley, P., Lohkamp, B., Scott, W. G. & Cowtan, K. Features and development of Coot. *Acta Crystallogr. Sect. D Biol. Crystallogr.* **66**, 486–501 (2010).
107. Ashkenazy, H. *et al.* ConSurf 2016: an improved methodology to estimate and visualize evolutionary conservation in macromolecules. *Nucleic Acids Res.* **44**, W344–W350 (2016).
108. Pettersen, E. F. *et al.* UCSF ChimeraX: Structure visualization for researchers, educators, and developers. *Protein Sci.* **30**, 70–82 (2021).
109. Morin, A. *et al.* Collaboration gets the most out of software. *Elife* **2013**, 1–6 (2013).

Acknowledgments

We thank Dr. James Fuller, Dr. Minglei Zhao, Dr. Navid Bavi, and Dr. Jingxian Li for valuable discussion and advice regarding cryo-EM data processing and model building. We thank Dr. Zhiqing Wang of the NCEF facility for assistance in cryo-EM data collection. This research was, in part, supported by the National Cancer Institute's National Cryo-EM Facility at the Frederick National Laboratory for Cancer Research under contract 75N91019D00024. We thank Dr. Maxwell Watkins and Dr. Jesse Hopkins for assistance in SAXS and MALS data collection and processing. This research used resources of the Advanced Photon Source, a U.S. Department of Energy (DOE) Office of Science User Facility operated for the DOE Office of Science by Argonne National Laboratory under Contract No. DE-AC02-06CH11357. BioCAT was supported by grant P30 GM138395 from the National Institute of General Medical Sciences of the National Institutes of Health. The mass photometry analysis was performed by the Biophysics Core in Research Resources Center of University of Illinois at Chicago. Software used in the project was installed and configured by SBGrid.[109] The content is solely the responsibility of the authors and does not necessarily reflect the official views of the National Institute of General Medical Sciences or the National Institutes of Health.

Figures and Tables

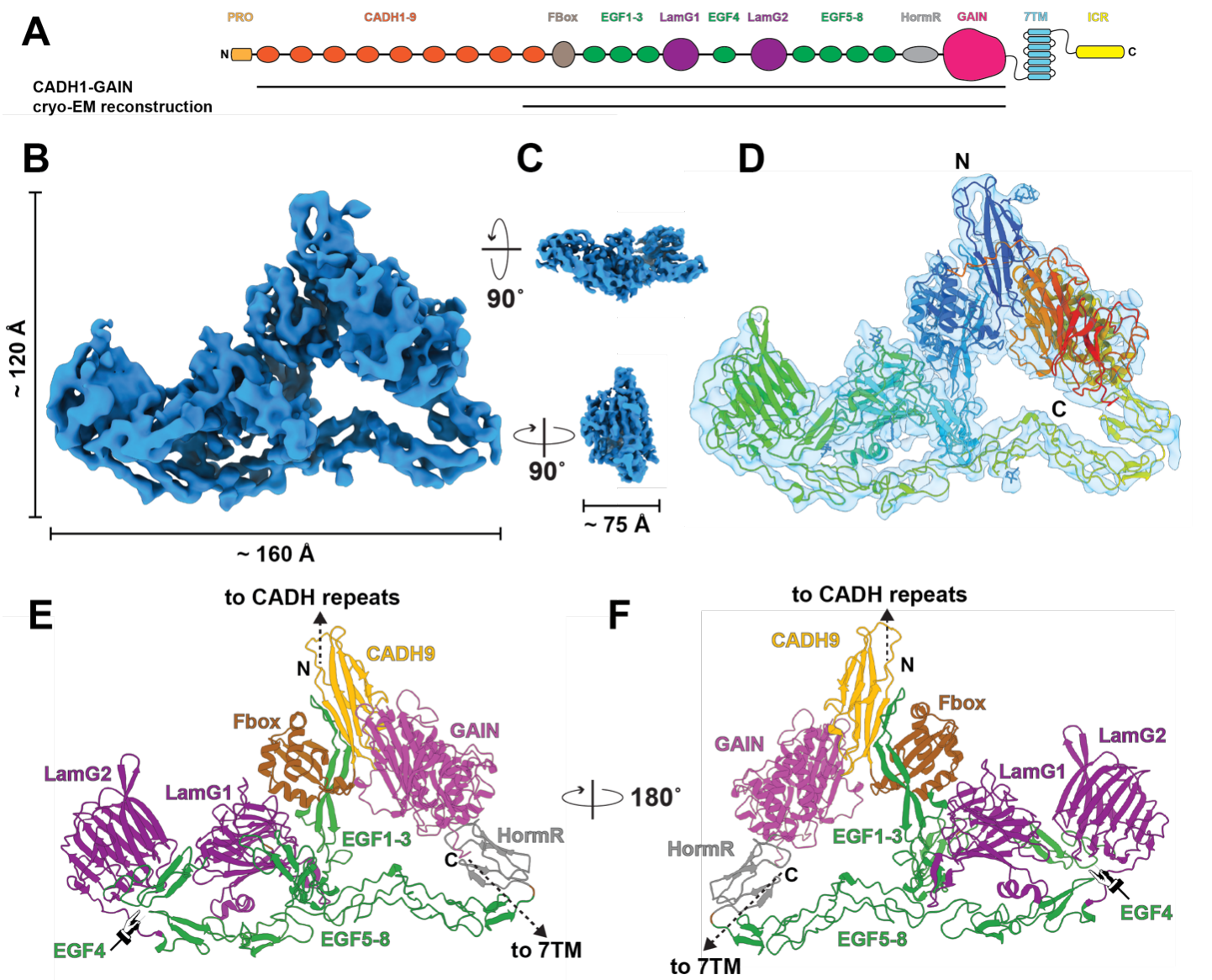

Fig. 1. The 4.3 Å Cryo-EM reconstruction of the extracellular region of mCELSR1 reveals a compact interdomain bundle including 13 domains. (A): A cartoon diagram shows the overall domain architecture of mCELSR1 with horizontal lines indicating boundaries used in the construct and the boundaries resolved in the reconstruction. PRO: prodomain; CADH: cadherin repeat; Fbox: Flamingo Box domain; EGF: epidermal growth factor repeat; LamG: laminin G repeat; HormR: hormone receptor domain; GAIN: GPCR autoproteolysis-inducing domain; 7TM: seven transmembrane region; ICR: intracellular region. **(B):** Coulomb potential map of the cryo-EM reconstruction reveals a compact triangular shape. **(C):** Orthogonal views of (B) illustrate that the overall shape of the density is flatter in one dimension vs. the other two. **(D):** A cartoon representation of the mCELSR1 ECR atomic model colored from blue (N-term) to red (C-term) is fit into the coulomb potential map and shows that the N-terminal portion of the structure interacts with the C-terminal portion. (**E) and (F)**: The atomic model for the mCELSR1 ECR is shown as a cartoon representation and domains are colored as in (A) to illustrate how the CADH9-GAIN domains are arranged in space.

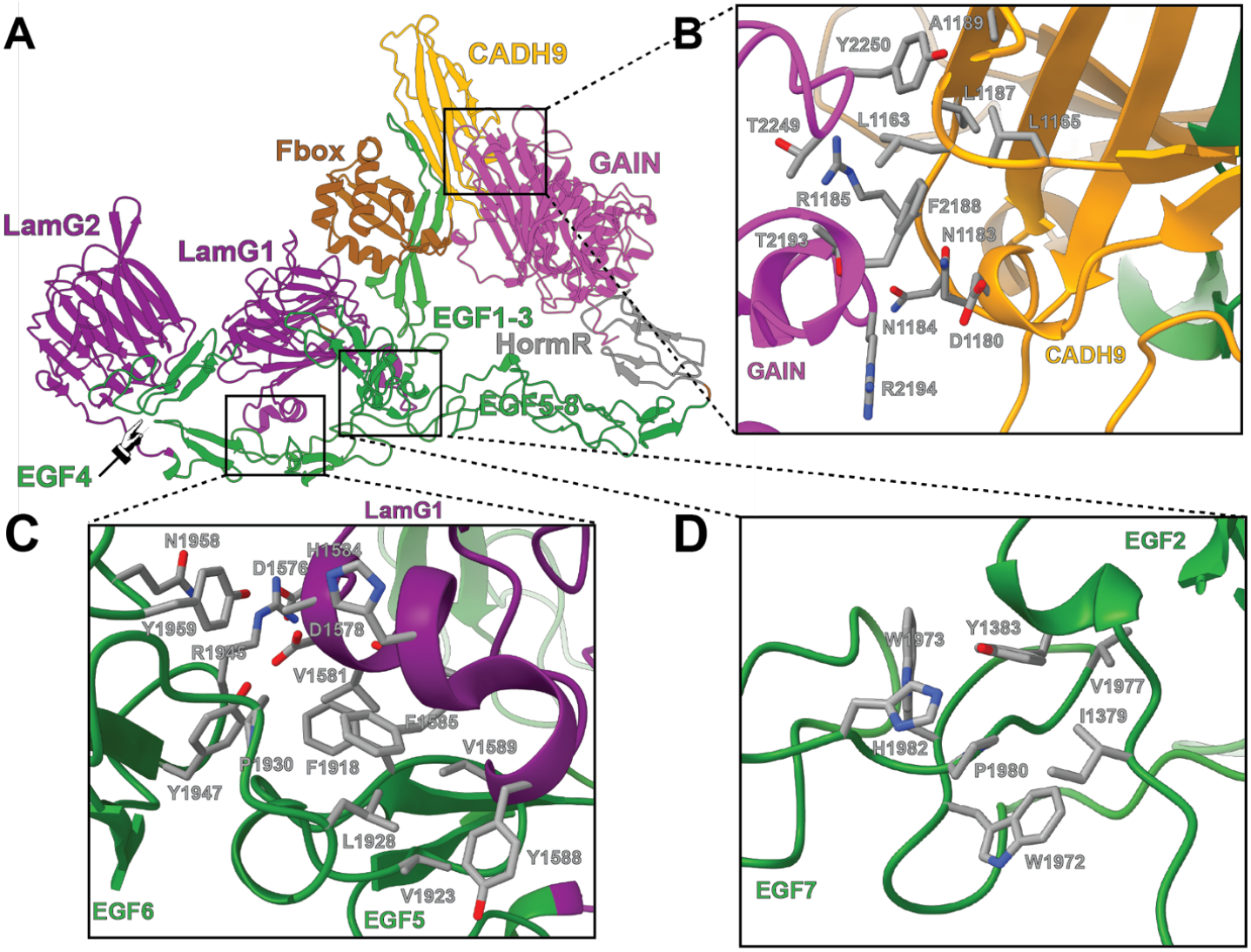

Fig. 2. Structural details of interdomain interfaces stabilizing the mCELSR1 ECR compact bundle. (A): Cartoon representation of mCELSR1 ECR structure with key interfaces enclosed in black rectangles. **(B):** Cartoon model showing the interface between CADH9 and GAIN domains. Important residues are shown as sticks. **(C):** Cartoon model showing the EGF5/EGF6/LamG1 interface with important residues shown as sticks. **(D):** Cartoon model showing the interface between EGF2 and EGF7 domains with important residues shown as sticks.

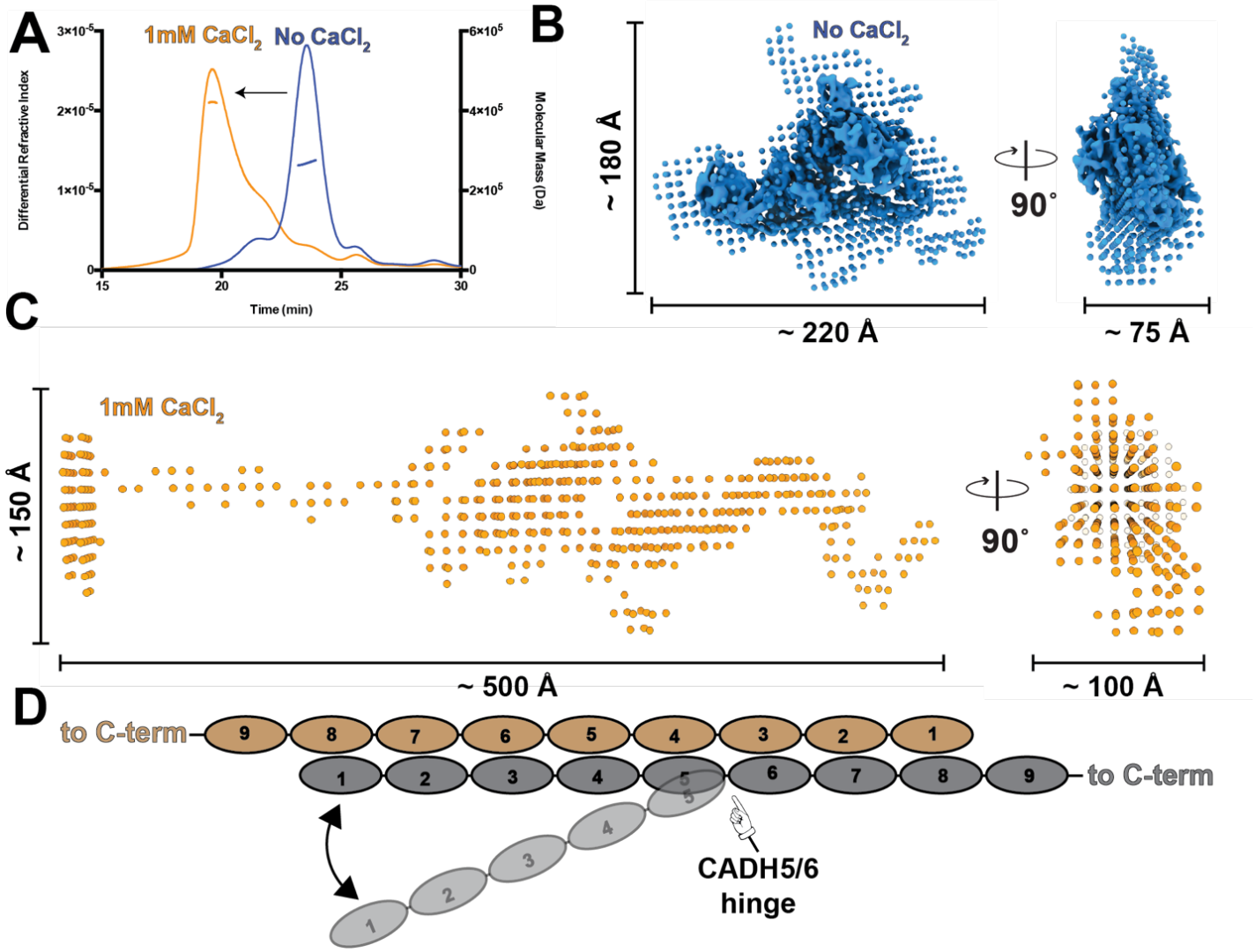

Fig. 3. SEC-MALS analysis of mCELSR1 CADH1-GAIN. (A): Overlay of SEC-MALS traces in the absence of $CaCl_2$ (blue curve) and in the presence of 1 mM $CaCl_2$ (orange curve). Using a Superose 6 column, a leftward shift of the elution volume is seen with 1mM $CaCl_2$, suggesting the presence of a Ca^{2+}-dependent dimer. Differential refractive index is plotted on the left and the calculated molecular mass is plotted on the right axis. The traces represent the differential refractive index whereas the horizontal lines in the peaks show the calculated molecular masses. **(B):** A bead model generated using DAMMIN/DAMMIF based on the No $CaCl_2$ SAXS curve agrees well with the cryo-EM coulomb potential map, suggesting that the CADH9-GAIN CMM exists in solution. An orthogonal view shows that the overall shape of the bead model is flat in one dimension relative to the other two. **(C):** A bead model generated using DAMMIN/DAMMIF based on the 1 mM $CaCl_2$ SAXS curve shows a large, extended structure much longer in one dimension. **(D):** A cartoon diagram with a hypothesis for how the CADH repeat region is arranged within the extended density observed in (C). The CADH5-CADH6 hinge is shown in the bottom protomer.

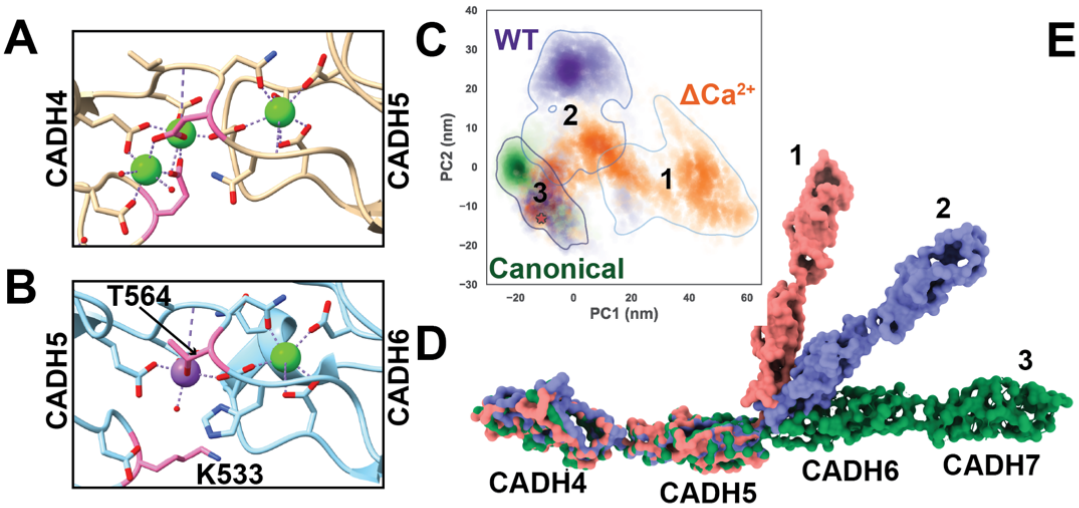

E

WT	1	9 %
WT	2	52 %
WT	3	39 %
ΔCa^{2+}	1	45 %
ΔCa^{2+}	2	23 %
ΔCa^{2+}	3	32 %
Canonical	1	0 %
Canonical	2	8 %
Canonical	3	92 %

Fig. 4. Molecular dynamics simulations on hCELSR1 CADH4-7 (PDB 7SZ8) support that a flexible hinge exists between CADH5 and CADH6. (A): A canonical calcium coordination site between CADH4 and CADH5 with 3 calcium ions coordinated. The protein backbone is shown as a cartoon, with key residues are shown as sticks with coordination shown as dotted lines. Calcium ions are shown as green spheres and water molecules are small red spheres. **(B):** The non-canonical calcium coordination site between CADH5 and CADH6 has two key anionic residues changed, T564 and K533 which are shown in pink. Shown as in (A) but with a bound sodium ion shown as a purple sphere. **(C):** Plot of simulation frames projected onto PC1-2 space, colored by condition (WT- purple, ΔCa^{2+} - orange, Canonical- green) and shaded by 2D kernel density estimate. A red star shows the start point of each simulation. Hierarchical clustering reveals shared dynamics between the three simulated conditions. **(D):** Each shown PDB model is a frame of the simulation that is closest to the centroid of the numbered cluster. **(E):** The percentage of time that each simulation spends in each cluster is presented on the right.

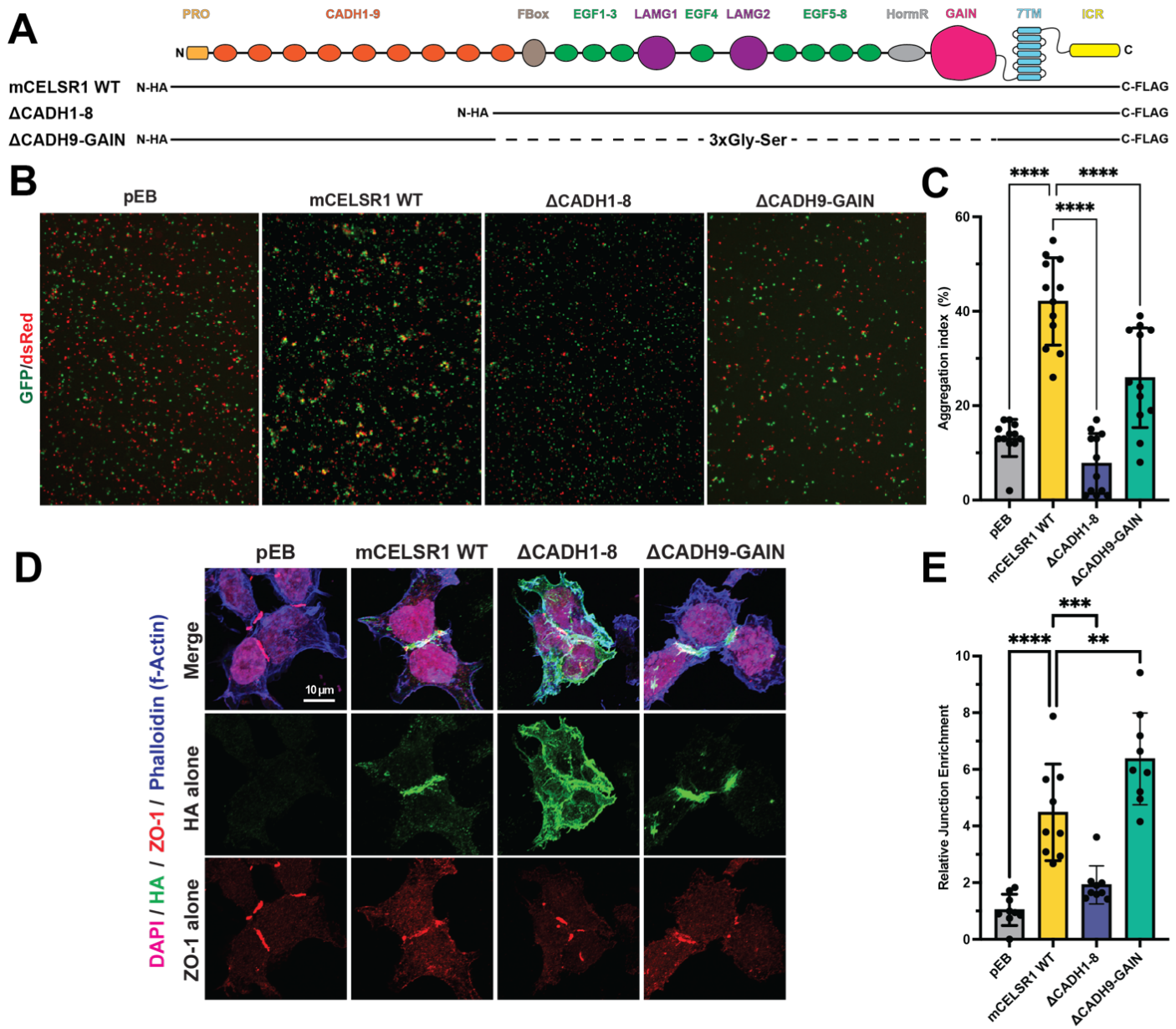

Fig. 5. Functional analysis of the adhesive properties of the mCELSR1 ECR. (A): Domain boundaries of constructs used in this study. Black solid lines show domain boundaries with dotted lines indicating regions that are connected with linkers. **(B):** Representative cell-cell aggregation assay images. Two cell populations were transfected with either GFP or dsRed and the noted constructs, and cells were imaged to assess aggregation. **(C):** Quantification of cell aggregation images as aggregation index. N=3 independent biological experiments each done in quadruplicate; each data point is shown. The average is plotted as a bar graph with standard deviation shown for the error bars. **(D):** Representative cell-cell junction enrichment assay images. Experimental constructs were imaged using the N-terminal HA tag (green). ZO-1 is used as a marker for the cell-cell junction (red), DAPI for the nucleus (pink), and phalloidin for filamentous actin (blue). **(E):** Quantification of images from (D) as relative junction enrichment. N=3 independent biological experiments each done in triplicate; graph as in (C). one-way ANOVA analysis with Dunnett's correction for multiple comparisons was performed to assess statistical significance between CELSR constructs. *** corresponds to $p = 0.0001$, **** corresponds to $p < 0.0001$.

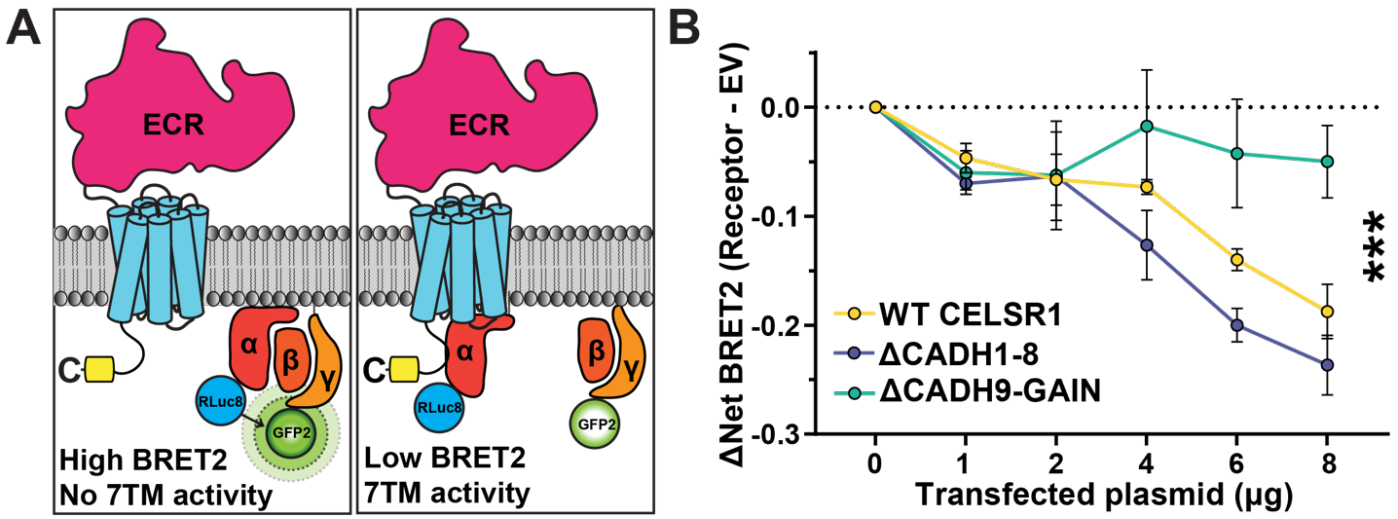

Fig. 6. G protein-coupling assay of mCELSR1 constructs using a Gα$_s$ BRET2 biosensor. (A): Cartoon describing the BRET2 biosensor assay. The ECR is shown as a magenta cartoon, the 7TM as cylinders for helices, and the intracellular region as a loop. The membrane is shown as head groups (circles) and lipid tail groups (serrated lines). Heterotrimeric G proteins are shown as cartoons and the BRET donor (RLuc8) and acceptor (GFP2) are shown as cartoons. **(B):** Change in net BRET2 is depicted vs. amount of transfected CELSR DNA construct. Each point represents N=3 independent experiments performed in triplicate. Two-way ANOVA analysis with Tukey's correction for multiple comparisons was performed to assess statistical significance between CELSR constructs. *** corresponds to p = 0.0001.

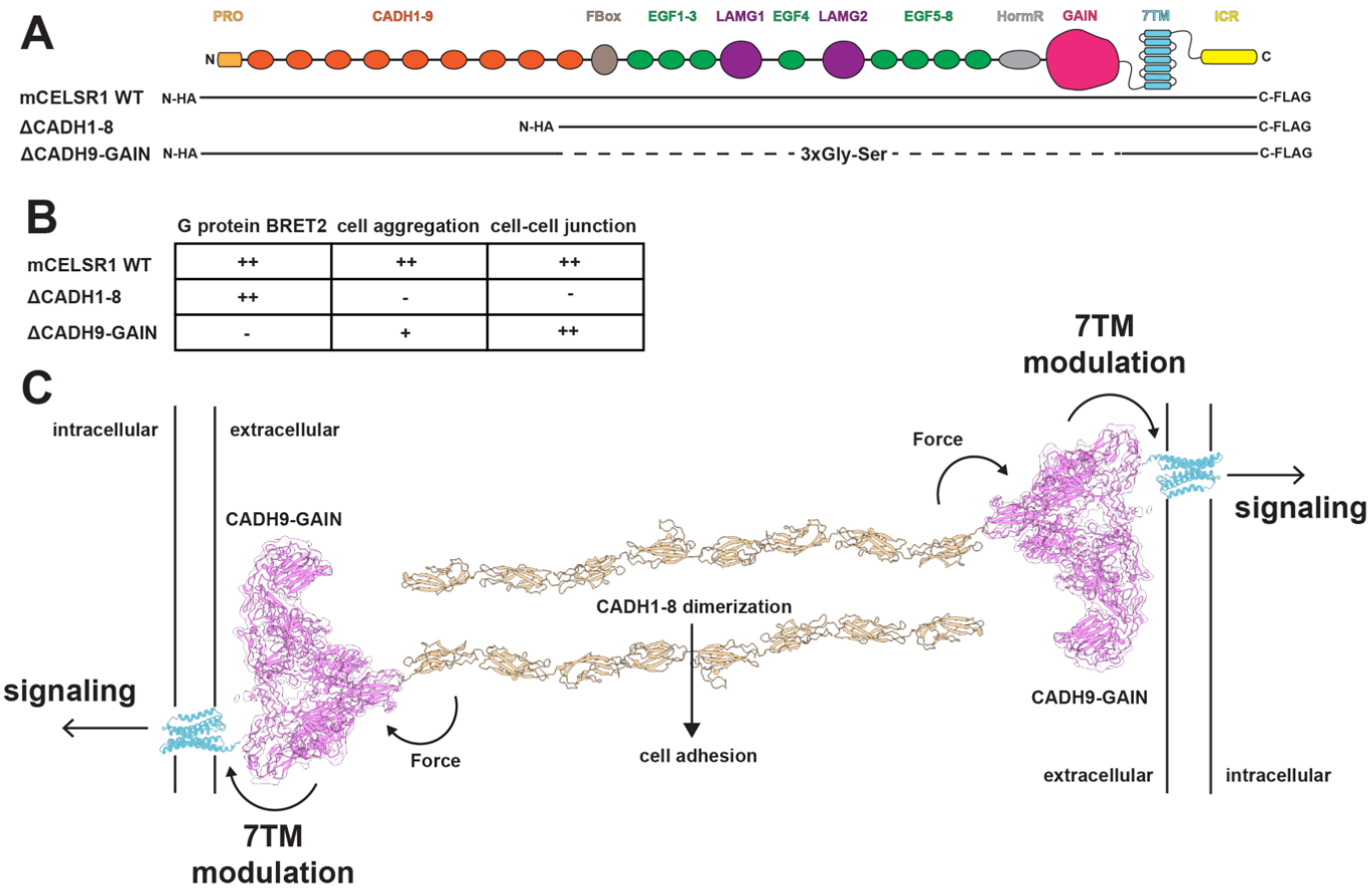

Fig. 7. Integrative model for function of CELSR1. The dimerization of cadherin repeat region, CADH1-8, leads to cell aggregation and localization to cell-cell junction. This adhesion can transmit a force to the CADH9-GAIN CMM, and the CADH9-GAIN bundle regulates signaling by communicating with the 7TM. **(A):** Construct diagram with black horizontal lines showing the domain boundaries of important constructs used in this work. **(B):** Summary table with the results of each assay shown as positives or negatives. **(C):** Cartoon model showing the trans nature of CELSR function.